Journal of Materials Chemistry A

ROYAL SOCIETY OF CHEMISTRY

COMMUNICATION

View Article Online
View Journal | View Issue

Cite this: J. Mater. Chem. A, 2020, 8, 17405

Received 12th June 2020
Accepted 3rd August 2020

DOI: 10.1039/d0ta05842d

rsc.li/materials-a

Pyrochlore nanocrystals as versatile quasi-single-source precursors to lithium conducting garnets†

J. Mark Weller [a] and Candace K. Chan *[ab]

Lithium conducting garnets are attractive solid electrolytes for solid-state lithium batteries but are difficult to process, generally requiring high reaction and sintering temperatures with long durations. In this work, we demonstrate a synthetic route to obtain Ta-doped garnet ($Li_{6.4}La_3Zr_{1.4}Ta_{0.6}O_{12}$) utilizing La- and Ta-doped lanthanum zirconate ($La_{2.4}Zr_{1.12}Ta_{0.48}O_{7.04}$) pyrochlore nanocrystals as quasi-single-source precursors. *Via* molten salt synthesis (MSS) in a highly basic flux, the pyrochlore nanocrystals transform to Li-garnet at reaction temperatures as low as 400 °C. We also show that the pyrochlore-to-garnet conversion can take place in one step using reactive sintering, resulting in densified garnet ceramics with high ionic conductivity (0.53 mS cm^{-1} at 21 °C) and relative density (up to 94.7%). This approach opens new avenues for lower temperature synthesis of lithium garnets using a quasi-single-source precursor and provides an alternative route to highly dense garnet solid electrolytes without requiring advanced sintering processes.

Garnet-type lithium lanthanum zirconate ($Li_7La_3Zr_2O_{12}$, LLZO) and its doped analogues are actively being explored as electrolytes for solid-state lithium batteries due to their beneficial properties (high ionic conductivity, electrochemical stability, inertness, *etc.*).[1] However, the synthesis and processing of LLZO is challenging, requiring high reaction temperatures (>900 °C and reaction times in excess of 8 h) when using conventional solid-state reaction (SSR) methods and binary oxide precursors (*e.g.*, La_2O_3, ZrO_2).[2,3] Recently, many synthesis strategies, such as sol–gel,[4,5] combustion,[6,7] and molten salt synthesis,[8–10] have focused on reducing the LLZO formation temperature. These methods often result in garnet powders with comparable properties to those synthesized *via* conventional SSR, but still generally require synthesis temperatures above 700 °C.[2,3]

One common feature of LLZO synthesis is the nearly ubiquitous presence of pyrochlore type lanthanum zirconate ($La_2Zr_2O_7$, LZO) as an intermediate phase before garnet formation, signalling incomplete reaction.[4–7,9,11] Its presence after extended calcination or sintering of LLZO indicates decomposition of the garnet structure due to evaporation of Li at high temperatures.[12] LZO beneficially contains the majority of the non-Li components of LLZO in a single crystalline phase. For this reason, some researchers have used it as a LLZO precursor. In one case, LLZO was synthesized from Li_2CO_3, $La(OH)_3$, and $La_2Zr_2O_7$,[13] but still required a temperature of 800 °C and only formed the low-conductivity[14] tetragonal ($I4_1/acd$) phase of garnet due to the absence of dopants needed to stabilize the high-conductivity[1] cubic ($Ia\bar{3}d$) phase. Devianna-poorani *et al.* used $La_2Zr_2O_7$ along with mixtures of nominal composition Li_7LaO_5 or $Li_{6.28}Al_{0.24}LaO_5$ to synthesize undoped and Al-doped cubic LLZO, but the resulting products were not phase-pure even with calcination at 1200 °C, which may have led to their lower ionic conductivity compared to LLZO synthesized using conventional precursors.[11] We speculate that the challenge in using LZO as a precursor for garnet synthesis is due in part to the difference in La : Zr stoichiometry between LZO and LLZO (1 : 1 and 3 : 2 moles per formula unit, respectively). One option to resolve this challenge is to obtain a La-excess pyrochlore phase that can also incorporate the dopants needed to stabilize the cubic garnet phase.

Pyrochlore-structured oxides generally display a high degree of flexibility in composition and substituents.[15] Pyrochlores adopt the general formula $A_2B_2O_6X$, where A = di- or trivalent cations, B = tetra- or pentavalent cations, and X = O^{2-}, OH^- or F^-.[15] The ease with which chemical substitutions can occur in pyrochlores is leveraged in this work, where we demonstrate the synthesis of ultrafine, nanocrystalline, multiply-doped LZO as a precursor for obtaining doped LLZO. Herein, we show that $La_{2+y}Zr_{2-x-y}Ta_xO_{7+(x-y)/2}$ nanocrystals can be synthesized with

[a]Materials Science and Engineering, School for Engineering of Matter, Transport and Energy, Arizona State University, P.O. Box 876106, Tempe, AZ 85827, USA. E-mail: candace.chan@asu.edu

[b]Department of Heterogeneous Catalysis, Max-Planck-Institut für Kohlenforschung, Kaiser-Wilhelm-Platz 1, 45470 Mülheim an der Ruhr, Germany

† Electronic supplementary information (ESI) available: Procedures for EIS fitting, tabulated data, XRD patterns, SEM images, S/TEM images and spectroscopic analyses, pair distribution function analysis, descriptions of synthesis and sintering conditions, and EIS data. See DOI: 10.1039/d0ta05842d

various amounts of Ta and excess La. The pyrochlore $La_{2.4}Zr_{1.12}Ta_{0.48}O_{7.04}$ (corresponding to a mole ratio of La : Zr : Ta = 3 : 1.4 : 0.6) is prepared and utilized as a quasi-single-source-precursor for the garnet ($Li_{6.4}La_3Zr_{1.4}Ta_{0.6}O_{12}$), requiring only a lithium source for the transformation. These pyrochlores can convert to garnets at reaction temperatures as low as 400 °C using molten salt synthesis (MSS) in a highly basic flux. Additionally, densified garnet ceramics can be formed directly from pyrochlore powders *via in situ* reactive sintering with LiOH.

The synthesis of pyrochlore nanocrystals was adapted from the molten hydroxide method[16,17] used for complex oxides. Several syntheses were performed at 400 °C (see ESI†) to determine the feasibility of the extensive doping required to convert LZO to LLZO with only the addition of a Li-source. Fig. 1a shows synchrotron X-ray diffraction (XRD) patterns of La-doped LZO, Ta-doped LZO, and La/Ta co-doped LZO of increasing doping levels. The broad features in the XRD data are due to the small crystallite[18] size of these pyrochlores. These results show that phase-pure Ta-doped pyrochlore of nominal composition $La_2Zr_{1.5}Ta_{0.5}O_{7.25}$ could be prepared without any noticeable impurities, indicating that Ta readily incorporates into LZO using this method. For La-doped LZO, a small amount of $La(OH)_3$ was observed in the XRD pattern, suggesting that fully doping LZO to a ratio of 3 La : 2 Zr is not feasible. Minor $La(OH)_3$ (also likely nanocrystalline based on the breadth of the Bragg peaks observed in Fig. 1a), was also observed in co-doped LZO of nominal compositions $La_{2.2}Zr_{1.575}Ta_{0.225}O_{7.0125}$ and $La_{2.4}Zr_{1.12}Ta_{0.48}O_{7.04}$. Synchrotron X-ray pair distribution function (PDF) analysis (Fig. 1b) of the $La_{2.4}Zr_{1.12}Ta_{0.48}O_{7.04}$ sample showed a better fit to the pyrochlore ($Fd\bar{3}m$) rather than the defect fluorite ($Fm\bar{3}m$) structure.[19] The PDF refinement also indicates that, besides minor amounts of $La(OH)_3$ (~9 wt%), all other constituents, including Ta and the rest of the excess La, are contained in a single pyrochlore phase. Transmission electron microscopy (TEM) characterization confirmed that the pyrochlore particles are on the order of 10–20 nm in size and highly crystalline (Fig. 1c and d). Fig. 1e shows a high-angle annular dark-field scanning transmission electron microscopy

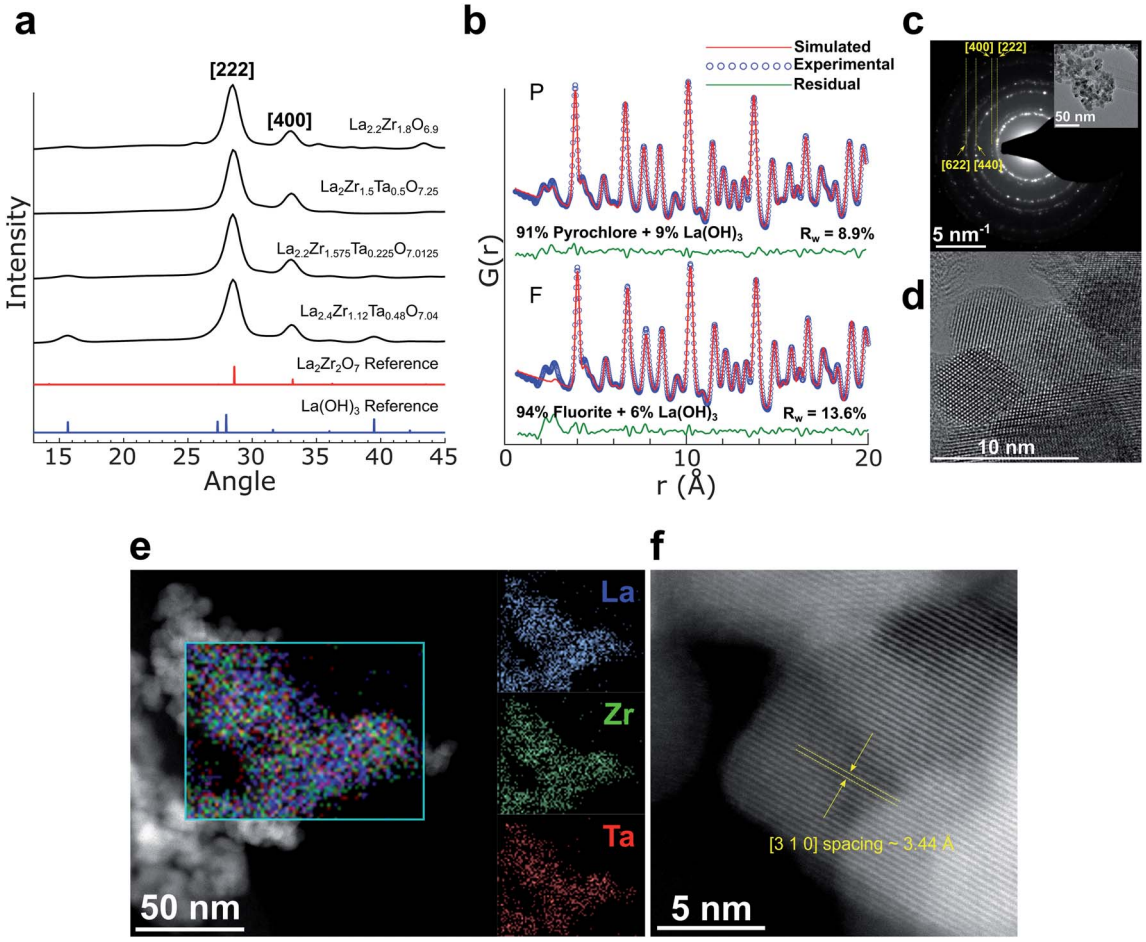

Fig. 1 Characterization of pyrochlore precursors. (a) Synchrotron XRD patterns of La/Ta co-doped LZO pyrochlores synthesized in molten hydroxides; (b) synchrotron X-ray PDF analysis of $La_{2.4}Zr_{1.12}Ta_{0.48}O_{7.04}$ showing the structure is a better fit to pyrochlore *vs.* defect fluorite with minimal $La(OH)_3$ as a secondary phase; (c) TEM electron diffraction ring pattern with major pyrochlore reflections indicated (low magnification TEM image in inset) and corresponding (d) high resolution TEM image of $La_2Zr_{1.5}Ta_{0.5}O_{7.25}$ nanocrystals; (e) HAADF-STEM image of $La_{2.4}Zr_{1.12}Ta_{0.48}O_{7.04}$ pyrochlores with EDS map from the region outlined in cyan showing distribution of La, Zr, and Ta throughout the nanocrystals; (f) high resolution HAADF-STEM image of pyrochlores in (e).

(HAADF-STEM) image of these pyrochlores with a composite energy dispersive X-ray spectroscopy (STEM-EDS) composition map and elemental maps for La, Zr, and Ta (see Fig. S1† for average EDS spectrum), demonstrating good uniformity of each species in the pyrochlores. A high resolution HAADF-STEM image (Fig. 1f) also confirms the high crystallinity of these pyrochlores.

These results show that the $La_{2.4}Zr_{1.12}Ta_{0.48}O_{7.04}$ pyrochlores contain the necessary La, Zr, and Ta to be used as quasi-single-source precursors for the synthesis of garnets of composition $Li_{6.4}La_3Zr_{1.4}Ta_{0.6}O_{12}$ (LLZTO). To obtain LLZTO particles, a ternary mixture of $LiNO_3$–LiOH–Li_2O_2 was used as the reaction medium in which to synthesize the garnet from the pyrochlores *via* MSS. This ternary mixture is characterized by high Lux-Flood basicity,[20,21] which is expected to enable a low oxide formation temperature[22,23] while also serving as the lithium source for the reaction and also has the advantage of mitigating[10] proton-exchange in the as-synthesized powder compared to neutral molten salt media such as eutectic LiCl–KCl. The reaction time (1–5 h), temperature (400–550 °C), and ratio of Li_2O_2 : LiOH ([0, 0.5, or 1] : 3.2) in the melt were varied to understand the minimum conditions (time, temperature, amount of Li_2O_2) that enable garnet formation from the pyrochlores (see ESI† for detailed procedures, Fig. S2† for XRD patterns, Table S1† for specific experimental conditions used). These experiments reveal that pyrochlore nanocrystals convert to garnet crystals at temperatures as low as 400 °C in 5 h, which to our knowledge is the lowest Li-garnet synthesis temperature to be reported. For comparison, our previous work showed that garnet synthesis in neutral LiCl–KCl molten salts required a reaction temperature of 850 (ref. 10) or 900 °C.[9] Full conversion of the pyrochlore precursor to the garnet phase was observed with increased reaction time, temperature, or Lux-Flood basicity of the melt (*i.e.*, increased amounts of Li_2O_2 for a fixed ratio of $LiNO_3$/LiOH of 1.1 : 3.2). The minimum conditions in which phase-pure garnet were obtained at each temperature are summarized in Table 1.

Interestingly, it appears that the Lux-Flood basicity of Li_2O_2 is not the sole driving force for the reduced garnet formation temperature using this method, as a comparable melt with Na_2O_2 replacing Li_2O_2 did not result in garnet formation (see Fig. S2c†). This indicates that the Li_2O_2 likely first decomposes into reactive Li_2O,[24] which in turn promotes formation of the garnet phase at low temperatures, indicating a potentially broader use of Li_2O_2 as a reactive Li-source for LLZO synthesis. Indeed, the primary difference between low (0.5 moles) and high (1 mole) Li_2O_2 compositions in Table 1 is that generally less reaction time is required for higher Li_2O_2 content, indicating that Li_2O_2 modulates the reactivity/reaction rate. These results also indicate that garnet synthesis from pyrochlores is kinetically faster than using conventional reagents. For comparison, garnet of the same composition was synthesized from $La(NO_3)_3$, $ZrOCl_2$, and Ta_2O_5 using MSS in the same melt; phase-pure garnet was obtained at 550 °C in 4 hours as in our previous work[10] (Fig. S3†). With the pyrochlore reagents, phase-pure garnet adopting the high-conductivity cubic ($Ia\bar{3}d$)[1] structure formed in the same melt composition at 550 °C with only 1 h of reaction time (Fig. 2a and Table 1). We surmise that the presence of all major cationic components (La, Zr, and Ta) other than Li as well as the high surface area of the pyrochlore nanocrystals enables this rapid conversion to the garnet phase. These particles are generally submicrometer in size from scanning electron microscopy (SEM) observation (Fig. 2b) and highly crystalline based on TEM analysis (Fig. 2c and d). The HAADF-STEM and EDS analysis (Fig. S4†) also shows the uniform distribution of La, Zr, and Ta throughout the particles. These results confirm that this approach can enable the preparation of submicron garnet powders from doped pyrochlore nanocrystals. SEM images from a subset of other reaction conditions are shown in Fig. S5,† showing that in general, when only the minimum reaction time required to form garnet is used, the particle size of the resultant garnet is comparable to that in Fig. 2b regardless of reaction temperature. For lower synthesis temperatures (*e.g.* 450 °C, Fig. S5a–d†), increasing the reaction time from 3 to 5 hours does not appreciably increase the particle size with most particles being <1 μm. However, particle sizes coarsen substantially for longer reaction times at higher temperature (*e.g.* 500 °C) where primary particles go from mostly <1 μm for a shorter reaction time of 3 h (Fig. S5e and f†) to mostly >1 μm for a longer reaction time (Fig. S5g and h†) of 5 h.

In addition to the aforementioned $Li_{6.4}La_3Zr_{1.4}Ta_{0.6}O_{12}$ composition, we find that other garnet compositions are also accessible from doped pyrochlores using this method. The oxygen sublattice may be doped with fluorine by using NaF as pyrochlore dopant, resulting in cubic garnet with nominal composition $Li_{6.375}La_3Zr_2O_{11.375}F_{0.625}$ (Fig. S6†). Additionally, a more highly doped garnet composition, $Li_{6.025}La_{2.75}Ca_{0.25}Zr_{1.4}Ta_{0.6}O_{11.375}F_{0.625}$, was formed from pyrochlores co-doped with calcium, tantalum, and fluorine (Fig. S7†). These results show that doping with elements that readily incorporate into the pyrochlore structure,[15,26] such as alkaline earths (*e.g.*, Ca, Sr), lanthanides (*e.g.*, La, Nd), tetra- and pentavalent transition metals (*e.g.*, Ti, Zr, Nb, Ta), and F^- or OH^-, may be possible using this approach. The F and Ca/Ta/F doped compositions were investigated as a proof-of-concept for assessing wider applicability of this pyrochlore-to-garnet synthesis method, but further investigation of electrochemical performance was only pursued for Ta-doped garnets.

Table 1 Experimental MSS conditions (minimum time for a given temperature and salt molar ratio) that lead to phase-pure $Li_{6.4}La_3Zr_{1.4}Ta_{0.6}O_{12}$ garnet from $La_{2.4}Zr_{1.12}Ta_{0.48}O_{7.04}$ pyrochlore quasi-single-source precursors

Reaction temperature (°C)	Reaction time (h)	Molten salt composition, $LiNO_3$: LiOH : Li_2O_2 molar ratio
400	5	1.1 : 3.2 : 1
450	3	1.1 : 3.2 : 1
500	3	1.1 : 3.2 : 0.5
	1	1.1 : 3.2 : 1
550	3	1.1 : 3.2 : 0.5
	1	1.1 : 3.2 : 1
	4[a]	1.1 : 3.2 : 1

[a] Garnet synthesized from individual reagents rather than doped pyrochlores.

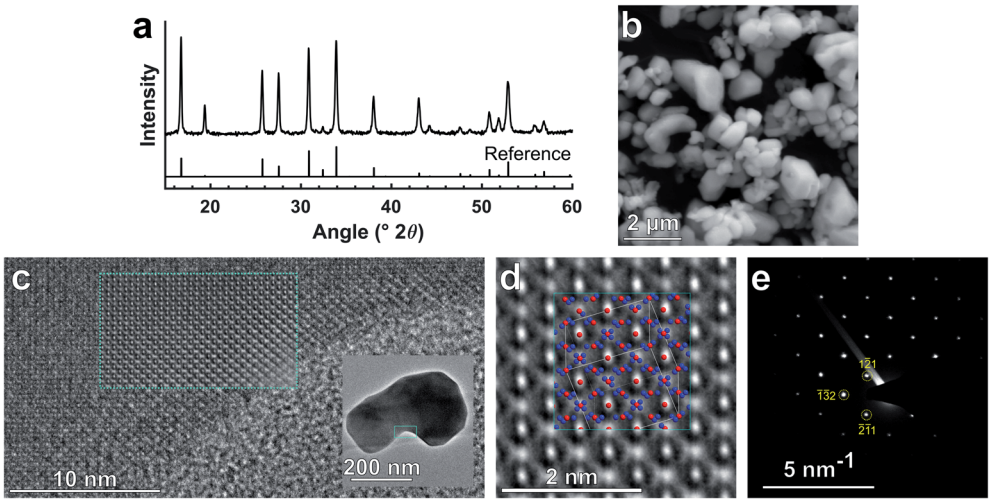

Fig. 2 Characterization of garnet synthesized from pyrochlore precursors (a) XRD pattern of $Li_{6.4}La_3Zr_{1.4}Ta_{0.6}O_{12}$ powder synthesized *via* MSS from pyrochlores (550 °C 1 h) with reference pattern (Logéat *et al.*),[25] (b) SEM image showing primarily submicron, faceted LLZTO crystals, (c) HRTEM image of fused LLZTO particle (synthesized at 500 °C for 3 h, low magnification image in inset) in ⟨135⟩ zone-axis orientation and Fourier-filtered image (cyan bordered region) overlaid to remove signal from amorphous carbon grid, (d) Fourier-filtered HRTEM image of (c) with [135] LLZTO crystal motif overlaid (La: blue, Zr/Ta: red), and (e) ⟨135⟩ zone-axis electron diffraction pattern of particle in (c) with select reflections indicated.

$Li_{6.4}La_3Zr_{1.4}Ta_{0.6}O_{12}$ garnet powders synthesized from pyrochlores were pressed and sintered at 1200 °C for 2 or 3 h followed by SEM fracture surface imaging and ionic conductivity analysis *via* electrochemical impedance spectroscopy (EIS) (see Table S2† for circuit fitting parameters). Fig. 3a shows an SEM fracture surface image of a garnet pellet after conventional sintering, revealing predominately transgranular fracture and large (20–50 μm) grains. Additionally, the quasi-single-source feature of the pyrochlore nanocrystals was also exploited for an alternative approach to obtain dense garnet electrolytes. In this case, the pyrochlores were blended with LiOH (10 mol% excess relative to the target garnet stoichiometry of $Li_{6.4}La_3Zr_{1.4}Ta_{0.6}O_{12}$) *via* ball-milling followed by pressing and sintering. In this reactive sintering approach, the reaction of LiOH with the pyrochlores during high temperature calcination results in simultaneous garnet formation and densification. Fig. 3b shows a fracture surface image of a reactively sintered pellet (1200 °C 3 h) revealing an extremely dense microstructure with small grains on the order of 2–5 μm and a relative density of 94.7%. Nyquist plots of symmetric cells using 20 wt% (1.5 mol%) Sn–Li alloy[27] electrodes are shown in Fig. 3c for both conventionally and reactively sintered garnets (1200 °C for 2 h, relative densities of 88.0% and 94.1% respectively) possessing room temperature (~21 °C) total ionic conductivities of 0.42 and 0.53 mS cm^{-1} respectively, comparable to those obtained from LLZTO prepared using standard SSR and other methods[7,10,28–41] (see Table S3† for detailed comparisons). No obvious grain boundary impedance is noticeable in the Nyquist plots in Fig. 3c, indicating that the tight grain structure from both sintering methods allows easy intergranular ion conduction. Finally, the activation energy of Li-ion conduction was determined from the temperature dependence of ionic conductivity (Fig. 3d, also see Fig. S8† for Nyquist plots at each temperature) for each sample to be 0.42 and 0.38 eV per atom for the conventionally and reactively sintered garnets respectively. The two processes described here for preparing garnet powders and ceramics from pyrochlores are illustrated schematically in Fig. 3e.

An XRD pattern of an LLZTO pellet formed from the reactive sintering approach is shown in Fig. S9† confirming that phase-pure garnet can be prepared from the pyrochlore powders directly using *in situ* reactive sintering without requiring an initial synthesis step. Another benefit to using pyrochlores and LiOH in this way is the inherent stability of both components with water, which eliminates challenges associated with Li^+/H^+ exchange[42,43] and subsequent carbonate formation,[42–46] which are also seen when using aqueous solutions[9,29,47] for processing garnets. Additionally, the microstructure and high relative density of the reactively sintered LLZTO resembles that of garnet sintered using hot-pressing,[30] spark-plasma sintering,[48] or Joule-heating induced rapid sintering.[49] This indicates that pyrochlore-to-garnet reactive sintering may enable comparable performance and properties without the more complex equipment required for these advanced sintering methods. Furthermore, reactive sintering is more generally applicable to processing of garnet solid-electrolytes in other forms such as thin films, where hot-pressing or spark-plasma sintering are not applicable. Such experiments are planned as future work.

In conclusion, a new synthesis approach is presented wherein doped $La_2Zr_2O_7$ pyrochlore nanocrystals are synthesized with a composition that will result in the correct stoichiometry to form Li-conducting garnets based on $Li_7La_3Zr_2O_{12}$. La and Ta co-doped pyrochlores with a La : Zr : Ta stoichiometry of 3 : 1.4 : 0.6 are demonstrated to readily form garnet-type $Li_{6.4}La_3Zr_{1.4}Ta_{0.6}O_{12}$ between 400–550 °C in a ternary mixture of molten $LiNO_3$–LiOH–Li_2O_2, with unprecedentedly low reaction temperatures. Pyrochlores can also be used as quasi-single-source precursors and blended with a Li source and reactively

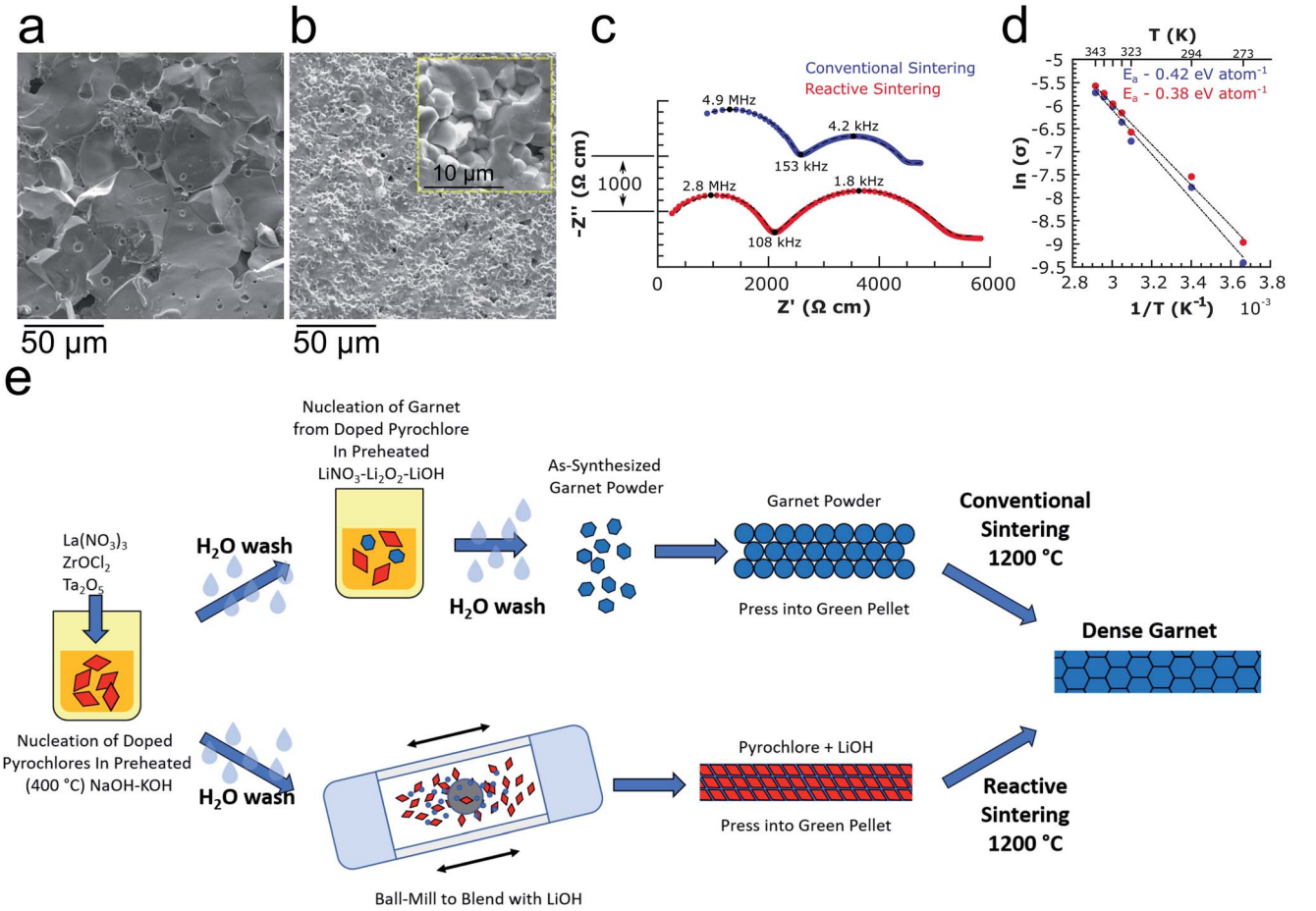

Fig. 3 Properties of garnet solid electrolytes resulting from the pyrochlore-to-garnet processes (a) SEM fracture surface image of a pellet sintered from LLZTO garnet powder synthesized from pyrochlore precursors (1200 °C, 3 h sintering time), (b) SEM fracture surface image of a reactively sintered pellet from pyrochlores + LiOH (1200 °C 3 h sintering time, higher magnification image in inset), (c) room temperature EIS spectra of conventionally and reactively sintered pellets (1200 °C, 2 h sintering time) with 1.5 mol% Sn–Li alloy electrodes (measured between 1 Hz and 7 MHz, impedance normalized to pellet dimensions, spectra are vertically offset for clarity with vertical axis scale shown), and (d) Arrhenius plots of ionic conductivity measured between 273–343 K for samples in (c) with activation energies determined to be 0.42 and 0.38 eV per atom for conventional and reactive sintering respectively. (e) Graphical depiction of workflow for using MSS to convert pyrochlores to garnets followed by conventional sintering (top), and for using *in situ* reactive sintering to form dense garnet ceramics directly from pyrochlores and a Li source such as LiOH (bottom).

sintered in 2 hours at 1200 °C to form highly dense, highly conducting garnet ceramics with a microstructure similar to that obtained through advanced sintering techniques, providing a unique and successful approach to dense garnet electrolytes that can be easily extended to more advanced ceramic forming techniques such as tape-casting or additive manufacturing, potentially improving processability of garnet solid-electrolytes for solid-state lithium batteries.

Conflicts of interest

There are no conflicts to declare.

Acknowledgements

This work was supported by the NSF CAREER award DMR 1553519. J. M. W. also acknowledges support from an ASU Fulton Schools of Engineering Dean's Fellowship and C. K. C. acknowledges support from the Max Planck Society as well as the Alexander von Humboldt Foundation for a Humboldt Research Fellowship. The authors gratefully acknowledge the use of facilities within the Eyring Materials Center at Arizona State University supported in part by NNCI-ECCS-1542160. The authors also thank Diamond Light Source (Didcot, UK) for access to beamline I15-1 (proposal no. CY23152, AP24) and D. Keeble for assistance with synchrotron measurements.

References

1 V. Thangadurai, S. Narayanan and D. Pinzaru, *Chem. Soc. Rev.*, 2014, **43**, 4714–4727.
2 S. Ramakumar, C. Deviannapoorani, L. Dhivya, L. S. Shankar and R. Murugan, *Prog. Mater. Sci.*, 2017, **88**, 325–411.
3 C. K. Chan, T. Yang and J. Mark Weller, *Electrochim. Acta*, 2017, **253**, 268–280.

4 J. Sakamoto, E. Rangasamy, H. Kim, Y. Kim and J. Wolfenstine, *Nanotechnology*, 2013, **24**, 424005.
5 N. Janani, S. Ramakumar, L. Dhivya, C. Deviannapoorani, K. Saranya and R. Murugan, *Ionics*, 2011, **17**, 575–580.
6 S. Afyon, F. Krumeich and J. L. M. Rupp, *J. Mater. Chem. A*, 2015, **3**, 18636–18648.
7 J. M. Weller, J. A. Whetten and C. K. Chan, *ACS Appl. Mater. Interfaces*, 2020, **12**, 953–962.
8 M. V. Reddy and S. Adams, *J. Solid State Electrochem.*, 2017, **21**, 2921–2928.
9 J. M. Weller, J. A. Whetten and C. K. Chan, *ACS Appl. Energy Mater.*, 2018, **1**, 552–560.
10 J. M. Weller and C. K. Chan, *ACS Appl. Energy Mater.*, 2020, **3**, 6466–6475.
11 C. Deviannapoorani, S. Ramakumar, N. Janani and R. Murugan, *Solid State Ionics*, 2015, **283**, 123–130.
12 E. Rangasamy, J. Wolfenstine and J. Sakamoto, *Solid State Ionics*, 2012, **206**, 28–32.
13 T. Kimura, Y. Yamada, K. Yamamoto, T. Matsuda, H. Nomura and T. Hirayama, *J. Am. Ceram. Soc.*, 2017, **100**, 1313–1319.
14 J. Awaka, N. Kijima, H. Hayakawa and J. Akimoto, *J. Solid State Chem.*, 2009, **182**, 2046–2052.
15 M. A. Subramanian, G. Aravamudan and G. V. S. Rao, *Prog. Solid State Chem.*, 1983, **15**, 55–143.
16 H. Liu, C. Hu and Z. L. Wang, *Nano Lett.*, 2006, **6**, 1535–1540.
17 H. Jin, D. Huang, Q. Gao, L. Li, N. Wang, Y. Wang and S. Hou, *Mater. Res. Bull.*, 2012, **47**, 51–53.
18 B. D. Cullity and S. R. Stock, *Elements of X-RAY DIFFRACTION*, 2nd edn, 1978.
19 B. Paul, K. Singh, T. Jaroń, A. Roy and A. Chowdhury, *J. Alloys Compd.*, 2016, **686**, 130–136.
20 H. Lux, *Z. Elektrochem.*, 1939, **45**, 303.
21 H. Flood and T. Förland, *Acta Chem. Scand.*, 1947, 592–604.
22 X. Liu, N. Fechler and M. Antonietti, *Chem. Soc. Rev.*, 2013, **42**, 8237.
23 Y. Du and D. Inman, *J. Mater. Sci.*, 1996, **31**, 5505–5511.
24 K. P. C. Yao, D. G. Kwabi, R. A. Quinlan, A. N. Mansour, A. Grimaud, Y. Lee, Y. Lu and Y. Shao-horn, *J. Electrochem. Soc.*, 2013, **160**, 824–831.
25 A. Logéat, T. Köhler, U. Eisele, B. Stiaszny, A. Harzer, M. Tovar, A. Senyshyn, H. Ehrenberg and B. Kozinsky, *Solid State Ionics*, 2012, **206**, 33–38.
26 A. A. Yaroshevskii and Y. A. Bagdasarov, *Geochem. Int.*, 2008, **46**, 1245–1266.
27 C. Wang, H. Xie, L. Zhang, Y. Gong, G. Pastel, J. Dai, B. Liu, E. D. Wachsman and L. Hu, *Adv. Energy Mater.*, 2018, **8**, 1701963.
28 X. Huang, Y. Lu, Z. Song, K. Rui, Q. Wang, T. Xiu, M. E. Badding and Z. Wen, *Energy Storage Materials*, 2019, **22**, 207–217.
29 X. Huang, Y. Lu, J. Jin, S. Gu, T. Xiu, Z. Song, M. E. Badding and Z. Wen, *ACS Appl. Mater. Interfaces*, 2018, **10**, 17147–17155.
30 T. Thompson, A. Sharafi, M. D. Johannes, A. Huq, J. L. Allen, J. Wolfenstine and J. Sakamoto, *Adv. Energy Mater.*, 2015, **5**, 1–9.
31 Y. Wang and W. Lai, *Electrochem. Solid-State Lett.*, 2012, **15**, A68.
32 M. Yi, T. Liu, X. Wang, J. Li, C. Wang and Y. Mo, *Ceram. Int.*, 2019, **45**, 786–792.
33 N. Janani, S. Ramakumar, S. Kannan and R. Murugan, *J. Am. Ceram. Soc.*, 2015, **98**, 2039–2046.
34 R. Inada, K. Kusakabe, T. Tanaka, S. Kudo and Y. Sakurai, *Solid State Ionics*, 2014, **262**, 568–572.
35 R. Inada, S. Yasuda, M. Tojo, K. Tsuritani, T. Tojo and Y. Sakurai, *Front. Energy Res.*, 2016, **4**, 1–12.
36 L. Dhivya and R. Murugan, *ACS Appl. Mater. Interfaces*, 2014, **6**, 17606–17615.
37 M. Huang, M. Shoji, Y. Shen, C. W. Nan, H. Munakata and K. Kanamura, *J. Power Sources*, 2014, **261**, 206–211.
38 C.-L. L. Tsai, V. Roddatis, C. V. Chandran, Q. Ma, S. Uhlenbruck, M. Bram, P. Heitjans and O. Guillon, *ACS Appl. Mater. Interfaces*, 2016, **8**, 10617–10626.
39 X. Chen, T. Cao, M. Xue, H. Lv, B. Li and C. Zhang, *Solid State Ionics*, 2018, **314**, 92–97.
40 X. Huang, T. Xiu, M. E. Badding and Z. Wen, *Ceram. Int.*, 2018, **44**, 5660–5667.
41 Y. Li, J. T. Han, C. A. Wang, H. Xie and J. B. Goodenough, *J. Mater. Chem.*, 2012, **22**, 15357–15361.
42 K. Hofstetter, A. J. Samson, S. Narayanan and V. Thangadurai, *J. Power Sources*, 2018, **390**, 297–312.
43 G. Larraz, a. Orera and M. L. Sanjuán, *J. Mater. Chem. A*, 2013, **1**, 11419.
44 L. Cheng, M. Liu, A. Mehta, H. L. Xin, F. Lin, K. A. Persson, G. Chen, E. J. Crumlin and M. M. Doeff, *ACS Appl. Energy Mater.*, 2018, **1**, 7244–7252.
45 H. Huo, J. Luo, V. Thangadurai, X. Guo, C. W. Nan and X. Sun, *ACS Energy Lett.*, 2020, **5**, 252–262.
46 L. Cheng, C. H. Wu, A. Jarry, W. Chen, Y. Ye, J. Zhu, R. Kostecki, K. Persson, J. Guo, M. Salmeron, G. Chen and M. Doeff, *ACS Appl. Mater. Interfaces*, 2015, **7**, 17649–17655.
47 R. Ye, C. Tsai, M. Ihrig, S. Sevinc, M. Rosen, E. Dashjav, Y. J. Sohn, E. Figgemeier and M. Finsterbusch, *Green Chem.*, 2020, **22**, 4952–4961.
48 H. Yamada, T. Ito and R. Hongahally Basappa, *Electrochim. Acta*, 2016, **222**, 648–656.
49 C. Wang, W. Ping, Q. Bai, H. Cui, R. Hensleigh, R. Wang, A. H. Brozena, Z. Xu, J. Dai, Y. Pei, C. Zheng, G. Pastel, J. Gao, X. Wang, H. Wang, J. Zhao, B. Yang, J. Luo, Y. Mo, B. Dunn and L. Hu, *Science*, 2020, **526**, 521–526.